M&C 2017 - International Conference on Mathematics & Computational Methods Applied to Nuclear Science & Engineering, Jeju, Korea, April 16-20, 2017, on USB (2017)

Multiphase Turbulence Mechanisms Identification from Consistent Analysis of Direct Numerical Simulation Data

B. Magolan, E. Baglietto
Department of Nuclear Science and Engineering, Massachusetts Institute of Technology, 77 Massachusetts Avenue 24-107, Cambridge, MA 02139, USA
bmagolan@mit.edu, emiliob@mit.edu

C. Brown, I.A. Bolotnov
Department of Nuclear Engineering, North Carolina State University, 2500 Stinson Drive, Raleigh, NC 27695, USA
csbrown3@ncsu.edu, igor_bolotnov@ncsu.edu

G. Tryggvason, J. Lu
Department of Aerospace and Mechanical Engineering, University of Notre Dame, Notre Dame, IN 46556, USA
gtryggva@nd.edu, jlu2@nd.edu

Abstract – *Direct Numerical Simulation (DNS) serves as an irreplaceable tool to probe the complexities of multiphase flow and identify turbulent mechanisms that elude conventional experimental measurement techniques. The insights unlocked via its careful analysis can be used to guide the formulation and development of turbulence models used in multiphase computational fluid dynamics (M-CFD) simulations of nuclear reactor applications. Here, we perform statistical analyses of DNS bubbly flow data generated by Bolotnov (Re_τ=400) and Lu & Tryggvason (Re_τ=150), examining single-point statistics of mean and turbulent liquid properties, turbulent kinetic energy budgets, and two-point correlations in space and time. Deformability of the bubble interface is shown to have a dramatic impact on the liquid turbulent stresses and energy budgets. A reduction in temporal and spatial correlations for the stream-wise turbulent stress (uu) is also observed at wall-normal distances of y^+=15, y/δ=0.5, and y/δ=1.0. These observations motivate the need for adaptation of length- and time-scales for bubble-induced turbulence models and serve as guidelines for future analyses of DNS bubbly flow data.*

I. INTRODUCTION

Understanding and predicting the fundamental two-phase flow and boiling heat transfer phenomena is instrumental to the thermal-hydraulic design and safety analysis of light-water reactors. Multiphase computational fluid dynamics (M-CFD) modeling techniques can be utilized to obtain predictions for these quantities. Such modeling approaches typically adopt the Eulerian-Eulerian two-fluid formulation [1] [2], which consists of solving a system of spatially and temporally averaged governing equations. By virtue of the averaging processes, additional terms arise that must be accounted for through prescription of suitable momentum and multiphase turbulent closure relations. The lack of consensus for the formulation of the multiphase turbulence closure relation comes as direct consequence of the incomplete understanding of the underlying physical phenomena. Therefore, before developing an advanced closure relation it is first necessary to identify the key multiphase turbulence mechanisms at play, which can be achieved by leveraging the volumes of statistics and data obtained from Direct Numerical Simulation (DNS) results.

The canonical multiphase turbulence model comprises the single-phase transport equations (e.g. k-ε, k-ω, SST) scaled by the liquid volume fraction. Notable efforts have been made to develop bubble-induced turbulent closure relation source terms in the turbulent transport equations [3] [4] [5] [6] [7]; however, in most cases these additions lead to worse prediction than the original formulations, and it is common practice in the industry to neglect such terms entirely. An effective multiphase turbulence model must revert back to the single-phase equations in the absence of vapor volume fraction; consequently, when searching for multiphase turbulence mechanisms one must be cognizant of how to incorporate these features into the model equations. Quantities that become of interest include turbulent time- and length-scales, as well as the turbulent kinetic energy budgets.

Experimental and DNS observations evidence several complex and interesting phenomena, associated with multiphase turbulence, that are lacking from current bubble-induced turbulence model formulations. While interfacial interactions generally act to augment the liquid turbulence profile, in high liquid flux / low gas flux flows liquid turbulence suppression has been routinely observed [8] [9] [10] [11] [12]. Further, spectral analyses of the liquid energy spectrum performed experimentally [9] [13] [14] and through DNS [15] [16] reveal that the well-established inertial range -5/3 power law, intrinsic to single-phase flows, is modified to a value close to -3 in multiphase flows; this suggests the need for modification to the rates of energy transfer and turbulent time-scales. Inspection of the turbulent kinetic energy budget terms has shown the impact of local volume fraction and relative velocity on the resulting liquid turbulence profile [17], as well as demonstrated enhanced production through

interfacial interaction, followed by immediate dissipation [18].

DNS has the potential to serve as an invaluable tool to probe these processes in order to identify and understand the complex multiphase turbulence mechanisms of interest. By resolving all time- and length-scales of the turbulent flow, DNS unlocks the ability to compute advanced statistics for turbulent quantities, turbulent kinetic energy budget terms, and turbulent scales. While these methods are computationally expensive and require large run-times on supercomputers, the insights that they can offer can be used to guide the development of enhanced multiphase turbulence models.

A great body of multiphase DNS has been performed for bubbly simulations of homogeneous flow [19] [20], parallel-plate [16] [18] [21] [22] [23], pipe [16], and reactor sub-channel geometries [16] [24]. Lu and Tryggvason [23] simulated over 100 bubbles in a vertical channel with Re_τ=250 and demonstrated the formation of a core region in hydrostatic equilibrium with the wall layer. Bolotnov [21] simulated 60 bubbles in a vertical channel with Re_τ=400 and examined the Reynolds stress components and resulting anisotropy distributions. More recently, advanced analysis techniques are beginning to be applied to bubbly flow simulations to improve understanding. Brown and Bolotnov [16] demonstrated the universality of the -3 power law in plate, pipe and reactor sub-channel geometries through frequency analysis of the energy spectrum using a linear interpolation between defective velocity signals. Santarelli et al. [18] performed a turbulent kinetic energy budget analysis of parallel plate geometry with Re_τ~170 and 2,880 bubbles, demonstrating a balance between interfacial turbulent production and the dissipation term that is an order of magnitude larger than single-phase observations. Ma et al. [25] have applied machine learning neural network techniques to develop the framework for optimization of closure relations and terms for the two-fluid model equations.

In this work, we examine DNS data presented by Bolotnov [21] and newly generated by Lu and Tryggvason in effort to identify multiphase turbulence mechanisms that can be used to inform the development of bubble-induced turbulent closure relations. Single-point statistics for mean and turbulent liquid quantities are first presented. Turbulent kinetic energy budget analyses for the production, dissipation, transport, and interfacial terms are then analyzed to trace how the multiphase flow influences the liquid turbulent kinetic energy distribution, and propagates through the equations. Next, two-point statistics are examined by computing auto-correlations and spatial correlations of the stream-wise (x) fluctuating velocity, at three wall-normal distances (y^+=15, y/δ=0.5, and y/δ=1.0), to assess the impact on the multiphase turbulence time- and length-scales, respectively.

II. DESCRIPTION OF THE WORK

The computational domain for both simulations involves a parallel-plate channel with no-slip conditions applied at the wall, and periodic boundary conditions applied in the stream-wise (x) and span-wise (z) directions (Fig. 1). Table I summarizes the key computational parameters and fluid properties adopted in the simulations. Definitions for all variables are provided in the Nomenclature section.

Table I. DNS Simulation Parameters

Parameter	Lu & Tryggvason	Bolotnov
Reference Name	LT	BOL
Code	custom	PHASTA
Domain Size (x,y,z)	π x 2 x π/2	2π x 2 x 2π/3
Mesh size (x,y,z)	384 x 256 x 192	587 x 187 x 195
Interface Resolution	Front Tracking	Level Set
Re_τ	150	400
Re	16,000	29,350
Eo	3.6	0.11
U_L	1.0	1.0
ρ_L	1.0	1.0
ρ_G	0.1	0.001208
ν_L	0.00025	0.000136
g	0.1	0.022
N_b	21	60
α	3.04%	1%
D_b/δ	0.3	0.25

1. DNS Data Format

A. Bolotnov

For each PHASTA simulation in Bolotnov [21], numerical probes were used to record instantaneous flow quantities that include phase, pressure, velocity, and velocity gradients. These virtual probes were distributed along the span-wise (z) and wall-normal directions (y) at two stream-wise (x) planar locations to gather sufficient statistics for calculation of the desired turbulent quantities (Fig. 1).

In this work we examine the ensemble-averaged flow statistics of 1 single-phase case and 5 two-phase cases with different bubble initializations. The single-phase case spanned 10,062 time-steps, which corresponds to 633,906 data points for each wall-normal (y) coordinate. Likewise, each two-phase run encompassed 6,036 time-steps, yielding 1,901,340 data points for each y-coordinate.

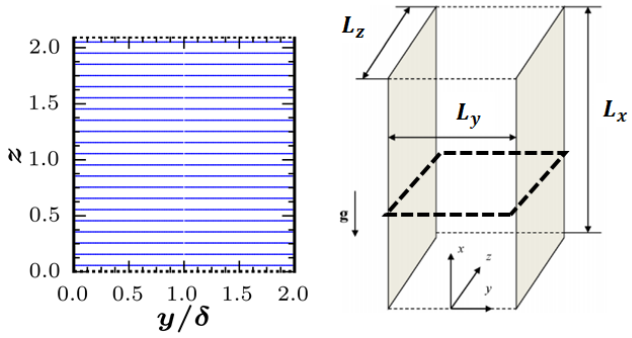

Fig. 1. Simulation domain (right) and distribution of numerical probes in stream-wise plane for Bolotnov cases (left). Walls are shown as shaded areas and periodic boundaries denoted by dashes.

A. Lu / Tryggvason

Access to the entire spatial domain values for velocity, pressure, and density, recorded every one second of computational time, was available for the LT data. Forty-six such full domain snapshots were examined, corresponding to 3,418,030 data points for each wall-normal (y) coordinate. Only two-phase data is examined here.

2. Methodology

By decomposing an arbitrary instantaneous quantity ($a_{i,k}$) into its mean ($\overline{\overline{A_{i,k}}}$) and fluctuating ($a'_{i,k}$) components it is possible to quantify the impact of turbulence on the flow profile. This phase-weighted average ($\overline{\overline{A_{i,k}}}$) is computed as [26]:

$$\overline{\overline{A_{i,k}}} = \frac{\overline{\Phi_k A_{i,k}}}{\overline{\Phi_k}} \tag{1}$$

Here, Φ_k is the phase indicator function that describes the presence of phase k at a given point in space ($\boldsymbol{x}$) and time (t):

$$\Phi_k(\boldsymbol{x},t) = \begin{cases} 1 & \text{if } (\boldsymbol{x},t) \text{ is occupied by phase } k \\ 0 & \text{otherwise} \end{cases} \tag{2}$$

The single over-bar ($\overline{\ }$) denotes a general averaging procedure with respect to time, space, or ensemble. In this study, such a quantity was computed by ensemble-averaging over a window of time-steps (t_w) for all probes/data points (p) in the span-wise (z) and stream-wise (x) directions in order to achieve a single, unique value for each wall-normal (y) coordinate in the domain. Following this convention, the averaged phase indicator function ($\overline{\Phi_k}$) at each y-coordinate was calculated as:

$$\overline{\Phi_k}(y) = \frac{1}{N_p N_w}\sum_{p=1}^{N_p}\left[\sum_{w=1}^{N_w}\Phi_k(\boldsymbol{x}_p, t_w)\right] \tag{3}$$

Note that this term is equivalent to the phase volume fraction (α_k).

A. Single-Point Statistics

Using the methodology outlined above, the phase-averaged single-point statistics for the mean velocity components (U_i) and turbulent Reynolds stresses (τ_{ij}) are defined as:

$$\overline{\overline{U_{i,k}}}(y) = \frac{1}{\alpha_k(y) N_p N_w}\sum_{p=1}^{N_p}\left[\sum_{w=1}^{N_w}\Phi_k u_{i,k}\right] \tag{4}$$

$$\overline{\overline{\tau_{ij,k}}}(y) = \frac{1}{\alpha_k(y) N_p N_w}\sum_{p=1}^{N_p}\left[\sum_{w=1}^{N_w}\Phi_k u'_{i,k} u'_{j,k}\right] \tag{5}$$

Note that all quantities in the summation terms above are functions of space and time ($\boldsymbol{x}_p$, t_w), and this notation has been omitted here for clarity. Lastly, the phase-averaged turbulent kinetic energy (k) is obtained by taking one half of the trace of the Reynolds stress tensor:

$$\overline{\overline{k_k}}(y) = \frac{1}{2\rho_k}\overline{\overline{\tau_{ii,k}}}(y) \tag{6}$$

B. Turbulent Kinetic Energy Budgets

For a fully-developed flow, the turbulent kinetic energy budget equation is defined as [3]:

$$0 = P + \epsilon + C + I \tag{7}$$

Analogous to the single-phase equations, the first three terms on the right-hand side denote liquid contributions to the turbulent kinetic energy budget by production (P) due to liquid shear, dissipation (ε) by viscosity, and diffusive transport (C) via viscous, pressure, and turbulent processes. The final term (I) represents the interfacial transport of turbulent kinetic energy arising from velocity fluctuations at the phase-boundary interface, which is grouped into pressure and viscous contributions. These four budget terms are calculated by applying the phase-weighted ensemble-averaging methodology outlined above and are defined below (note the omission of subscript L denoting the liquid phase for the sake of clarity here):

$$P = -\alpha\,\overline{\overline{u'_i u'_j}}\frac{\partial\overline{\overline{U_i}}}{\partial x_j} \tag{8}$$

$$\epsilon = -2\alpha\nu\,\overline{\overline{\frac{\partial u'_i}{\partial x_j}\frac{\partial u'_i}{\partial x_j}}} \tag{9}$$

$$C = \frac{1}{\rho}\frac{\partial\left(\alpha\overline{\overline{u'_i\tau'_{ij}}}\right)}{\partial x_j} - \frac{1}{\rho}\frac{\partial\left(\alpha\overline{\overline{p'u'_i}}\right)}{\partial x_i} - \frac{1}{2}\frac{\partial\left(\alpha\overline{\overline{u'_i u'_i u'_j}}\right)}{\partial x_j} \tag{10}$$

$$I = -\frac{1}{\rho}\overline{p' u_i' n_i S} + \frac{1}{\rho}\overline{\tau_{ij}' u_i' n_j S} \quad (11)$$

Here, n_i is the outward normal vector emanating from the phase-boundary interface, S is the interfacial area concentration, and τ_{ij}' is the fluctuating component of the viscous stress tensor (different from the Reynolds stress tensor):

$$\tau_{ij}' = \nu\left(\frac{\partial u_i'}{\partial x_j} + \frac{\partial u_j'}{\partial x_i}\right) \quad (12)$$

Only the production and dissipation terms can be computed for the BOL cases as the numerical probe data is distributed among two planes normal to the stream-wise direction and therefore does not have sufficient spatial resolution to compute the requisite gradients of the turbulent quantities; however, as the LT case comprises data spanning the entire spatial domain, it is indeed possible to compute the transport (C) and interfacial (I) terms using a centered difference gradient calculation scheme. The quantity $n_i S$ was approximated by computing the gradient of the phase indicator function using the expression derived by Kataoka et al. [27]:

$$\frac{\partial \Phi}{\partial x_i} = -n_i S \quad (13)$$

C. Two-Point Statistics

The two-point correlation function quantifies the relationship between fluctuating velocity components that are separated temporally (Eq. 14) or spatially (Eq. 15). When the magnitude of separation is zero, the correlation is unity, and ultimately tends to zero as the separation distance is increased.

$$R_{ij}(\tau) = \frac{\overline{u_i'(t) u_j'(t+\tau)}}{\overline{u_i'(t) u_{ij}'(t)}} \quad (14)$$

$$R_{ij}(\boldsymbol{x}) = \frac{\overline{u_i'(x) u_j'(x+r)}}{\overline{u_i'(x) u_j'(x)}} \quad (15)$$

Integration of the auto-correlation curve provides an estimate for the integral time-scale of turbulence (Eq. 16). Correspondingly, integration of the area under the spatial correlation curve provides an estimate for the integral turbulent length-scale (Eq. 17), which describes the size of the largest turbulent eddies present in the flow. Computation of the integral was carried out until the first zero was reached or if a local minimum was reached.

$$T = \int_0^\infty R(t')dt \quad (16)$$

$$L = \int_0^\infty R(x')dx \quad (17)$$

III. RESULTS

A side by side examination of the Bolotnov (BOL) and Lu/Tryggvason (LT) data for the turbulent quantities outlined above is performed here, to facilitate comparison between runs. When applicable, results are compared alongside with the Kasagi single-phase database for the same Re_τ [28].

1. Single-Point Statistics

The stream-wise liquid velocities—normalized by the friction velocity (u_τ)—and gas volume fraction (α_G) as a function of wall-normal distance (y) are plotted in Fig. 2. As can be seen, the BOL two-phase cases exhibit a wall-peaked volume fraction distribution whereas the LT case is center-peaked, a direct consequence of the imposed Eötvös number (Table I). Both the BOL and LT cases display a reduction in the liquid velocity by comparison to its single-phase profile.

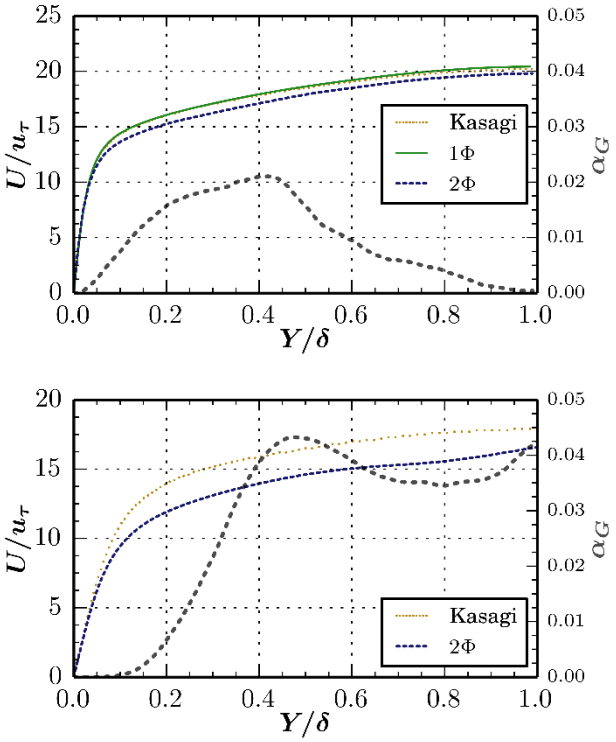

Fig. 2. Liquid mean velocity and gas volume fraction profiles for BOL (top) and LT (bottom) data.

The turbulent Reynolds stresses (uu, vv, ww, and uv) normalized by the square of the friction velocity (u_τ^2) are plotted in Fig. 3. The BOL two-phase data show only moderate augmentation of these terms in the near-wall region, with no appreciable impact in the center of the channel. Conversely, the LT data show a dramatic augmentation of all four Reynolds stress components throughout the entirety of the domain.

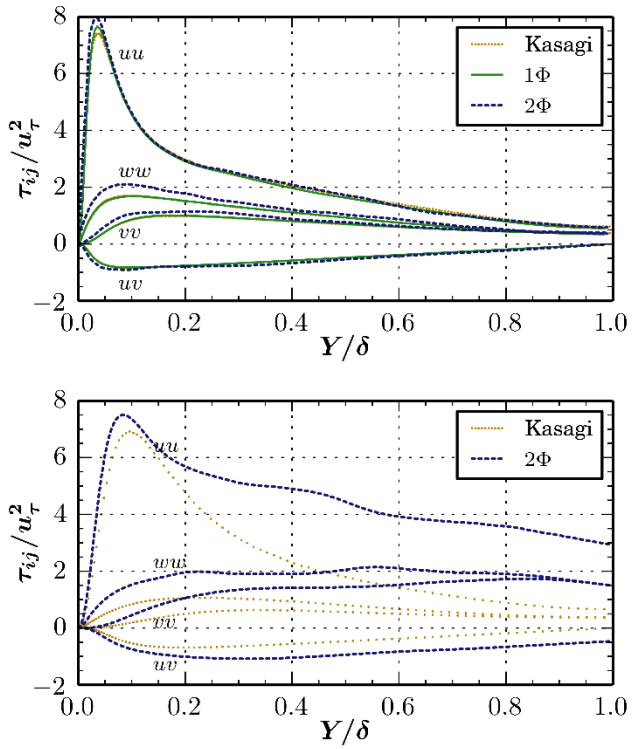

Fig. 3. Liquid turbulent Reynolds stresses for BOL (top) and LT (bottom) data.

2. Turbulent Kinetic Energy Budgets

The turbulent kinetic energy budgets (normalized by u_τ^4/ν) are presented in Fig. 4. For the BOL data, it is only possible to examine the production (P) and dissipation (ε) terms, due to the nature of the numerical probe data distributed at a select number of locations. The two-phase data show a slight increase in production due to liquid shear in the near-wall region, with minimal impact everywhere else in the domain.

Analysis of the LT case reveals a more dramatic modification of the turbulent kinetic energy budgets. A reduction in production throughout the domain is observed, with minimal impact on transport. There is a considerable increase in dissipation, which is balanced by the interfacial term in the bulk of the flow. Lastly, a residual term (*Res*) is also plotted to assess the balance of these four mechanisms ($P+\varepsilon+C+I$). This sum should approach zero given sufficient statistics and proper calculation of the budget terms (Eq. 7). In the bulk of the flow the *Res* term does indeed approach zero; however, when approaching the wall this residual error term increases, which implies that additional statistics are needed. Simulations remain underway to continue gathering statistics for these terms.

The prescribed Eötvös number ($\Delta\rho g D_b^2/\sigma$) is the primary difference between the BOL and LT cases. This term ranks the relative strengths of buoyancy and surface tension, with low values characterizing spherically shaped bubbles and higher values describing higher degrees of bubble deformability. The LT case is characterized by highly deformable bubbles (Eo = 3.6) whereas the BOL case has spherical bubbles (Eo = 0.11); it would therefore appear that the malleability of the phase-boundary interface imparts stronger fluctuations onto the liquid velocity components and their gradients, thereby augmenting these interfacial and dissipation terms. This observation further suggests that bubble deformability leads to a new quasi-equilibrium balance between interfacial transfer and dissipation mechanisms, which represents a transition from the production and dissipation balance intrinsic to single-phase flows.

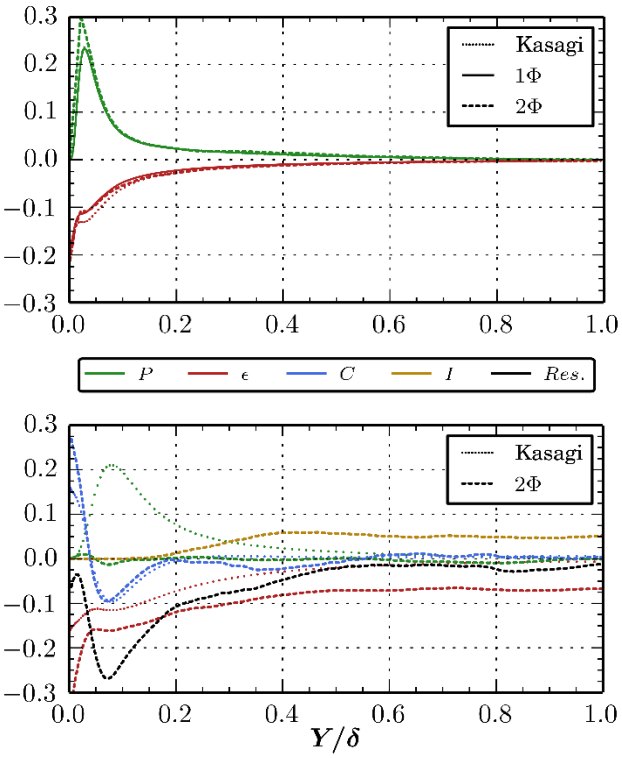

Fig. 4. Liquid turbulent kinetic energy budgets for BOL (top) and LT (bottom) data.

3. Two-Point Statistics

Two-point spatial and temporal correlations for *uu* at wall-normal distances of y^+=15, y/δ = 0.5, and y/δ =1.0 are examined here for the BOL and LT cases. The three-step process of (1) computing the correlation for each probe at a given wall-normal distance, (2) ensemble-averaging to yield a single representative curve, and (3) integrating to obtain an estimate for the turbulent scale is showcased in Fig. 5, where the auto-correlation of *uu* at y^+=15 for the BOL data is examined. As can be seen, the two-phase auto-correlation

curves (colored in gray) exhibit a much larger deviation in the behavior between numerical probes, which brings into question the validity of this approach and warrants further evaluation.

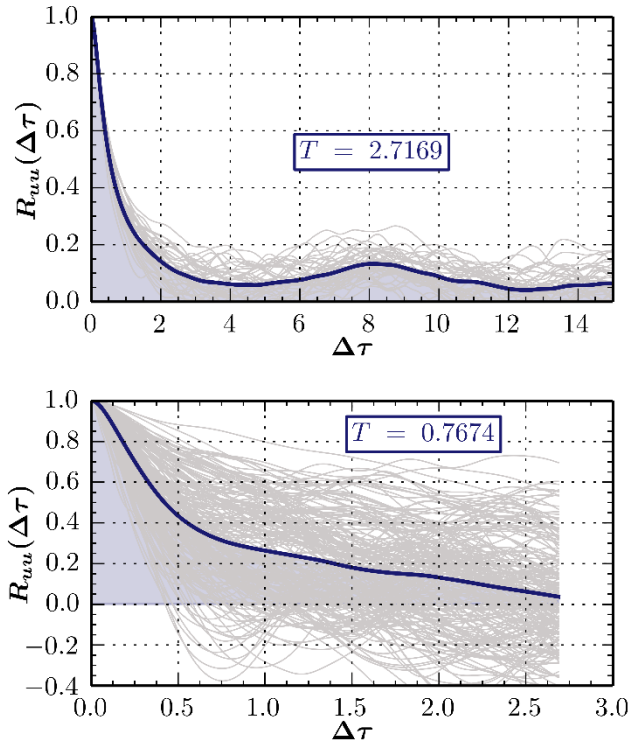

Fig. 5. Process for calculation of auto-correlation and integral time-scale at y^+=15 for BOL single-phase (top) and two-phase (bottom) cases. The gray curves denote auto-correlation for each probe, with the blue curve being the ensemble-averaged result used to compute the time-scale (*T*).

A. Temporal Correlations

The ensemble-averaged auto-correlation profiles for *uu* evaluated at y^+=15, y/δ = 0.5, and y/δ =1.0 are shown in Fig. 6 for the BOL data. Both the single- and two-phase cases display the trend of curves decreasing with increasing wall separation, with the two-phase cases slightly reduced by comparison to the single-phase values. These observations suggest a small reduction in the integral times-scale, which is physically justified by the interaction of the bubbles with the liquid velocity profile.

B. Spatial Correlations

The ensemble-averaged spatial correlation profiles for *uu* evaluated at y^+=15, y/δ = 0.5, and y/δ =1.0 in the span-wise (*z*) direction are shown in Fig. 7 for the BOL and LT data. Comparing across y-coordinate values, one observes the general trend of the correlation curves to increase with wall-normal distance; this finding is consistent with the presence of larger turbulent structures in the bulk of the flow.

The BOL cases show negligible difference between single- and two-phase cases at y^+=15. However, at y/δ = 0.5 and y/δ =1.0 the BOL two-phase results begin to deviate from their single-phase counterparts at a spatial separation ($\Delta z/\delta$) near 0.3, as evidenced by a reduction in their curves that attain a more negative value; it is worth noting that this spatial separation is slightly larger than one bubble diameter.

A reduction in the two-phase curves is observed for all three wall-normal distances for the LT case. The curves show larger oscillations than what is observed with the BOL data, which is attributable to the insufficient statistics.

Since data for the entire domain are available for the LT case, it is possible to further examine the spatial correlation in the stream-wise direction. Inspection of Fig. 8 reveals that increasing wall distance leads to a reduced correlation curve, which is opposite to the trend observed in the span-wise direction. This seemingly contradictory phenomena arises from the fact that long, narrow turbulent streaks and rolls are generated at the wall by liquid shear; as these structures are ejected from the wall into the bulk, they subsequently break up into smaller structures in the stream-wise direction, while simultaneously spreading out in the span-wise direction.

As with the span-wise direction, the stream-wise two-phase correlation curves are reduced by comparison to their single-phase values. This is observed for all three wall-normal distances and is most noticeable in the center of the channel (y/δ =1.0) where there the highest bubble concentration is observed (Fig. 2). Again, the curves exhibit some fluctuations, which suggests insufficient statistics for converged steady-state analysis. This simulation is ongoing and results will be updated upon receipt of additional data.

In summary, the reduction in the spatial correlation for *uu* in the stream-wise and span-wise directions for the two-phase DNS cases signifies a reduction in the integral length-scale of turbulence. This observation is expected, and it is attributed to the interfacial interactions between bubbles and the liquid phase.

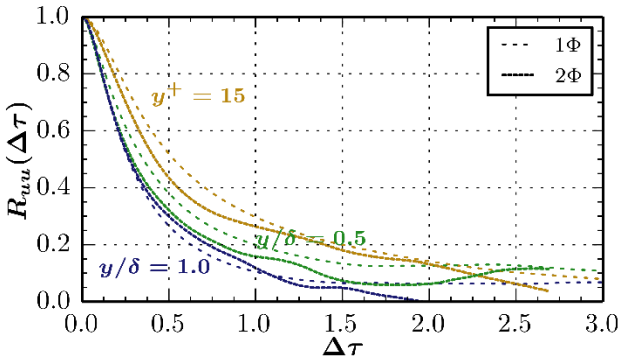

Fig. 6. Ensemble-averaged auto-correlation curve for *uu* at y^+=15, y/δ = 0.5, and y/δ =1.0 for BOL data.

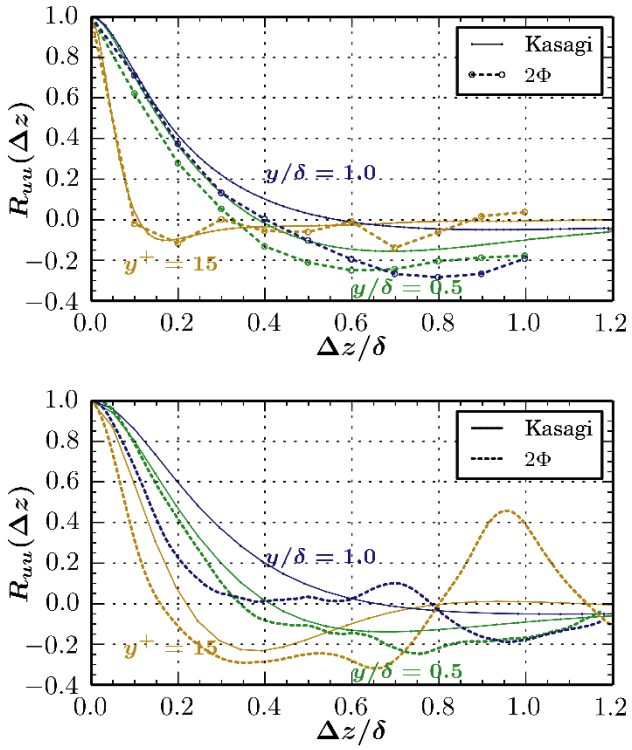

Fig. 7. Span-wise spatial correlations of *uu* at y^+=15, y/δ = 0.5, and y/δ =1.0 for BOL (top) and LT (bottom) data.

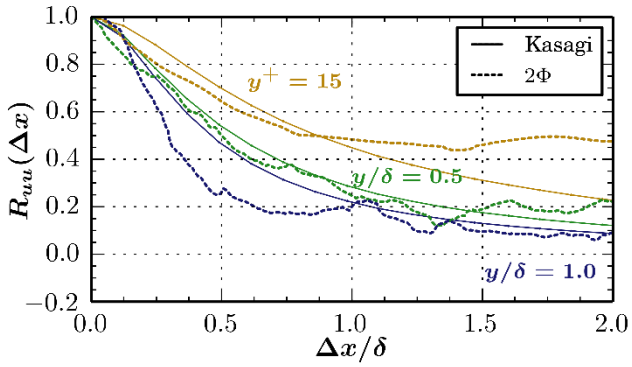

Fig. 8. Stream-wise spatial correlations of *uu* at y^+=15, y/δ = 0.5, and y/δ =1.0 for LT data.

IV. CONCLUSIONS

Examination of bubbly flow DNS data generated by Bolotnov (BOL) and Lu/Tryggvason (LT) suggests that bubble deformability at the phase-boundary interface serves an important role in the liquid turbulent kinetic energy profile. Inspection of the turbulent stresses for BOL (spherical bubbles) shows slight augmentation in the near-wall region, whereas LT (deformable bubbles) shows dramatic augmentation throughout the domain.

Analysis of the turbulent kinetic energy budget terms further supports this notion, wherein the BOL two-phase production and dissipation terms show minimal deviation from their single-phase values. On the other hand, the LT two-phase data exhibit a considerable reduction in production, and a dramatic increase in dissipation that is in balance with the interfacial transfer term in the bulk of the flow. Together, these observations suggest that the quasi-equilibrium turbulent kinetic energy balance between production and dissipation that is intrinsic to single-phase flows undergoes a transition to form a new balance between interfacial transfer and dissipation. This observation has also been confirmed experimentally [17] and in previous numerical studies [18].

Reduction of the two-phase temporal and spatial correlation curves, calculated at three wall-normal distances, further implies the reduction of turbulent length- and time-scales. This latter statement will require further confirmation, as the DNS data for the LT case still had insufficient statistics, which led to fluctuations in the computed curves. This simulation is ongoing and the results and analysis will be updated accordingly.

The observations brought forward in this work provide the base to support the development of M-CFD turbulence models through modification and scaling of the bubble-induced turbulent source terms, which arise in both the *k* and *ε* transport equations. Future DNS research endeavors will investigate the individual tensor components of the budget terms, in addition to expanding the parameter space by further examination of the Re_τ and *Eo* impact the liquid turbulent profile.

NOMENCLATURE

g = gravity
i = velocity / tensor component
j = velocity / tensor component
k = phase / turbulent kinetic energy
n = direction normal to phase interface
p = pressure / probe index
r = spatial separation
t_w = time-step
u_τ = friction velocity
x = position

C = transport of turbulent kinetic energy
D_b = bubble diameter
Eo = Eötvös number
G = gas phase
I = interfacial transfer of turbulent kinetic energy
L = liquid phase
P = production of turbulent kinetic energy
N_b = number of bubbles in domain
N_p = number of probes/data points in averaging window
N_w = number of time-steps in averaging window
Re = Reynolds number
Re_τ = Reynolds number based on friction velocity

S = interfacial area concentration

α = volume fraction
δ = channel half-width
ε = dissipation of turbulent kinetic energy
ρ = density
Φ = phase indicator function
τ = increment in time
τ_{ij} = Reynolds stress tensor
τ_{ij}' = fluctuating viscous stress tensor
ν = kinematic viscosity

ACKNOWLEDGMENTS

This research was performed under appointment to the Rickover Fellowship Program in Nuclear Engineering sponsored by Naval Reactors Division of the National Nuclear Security Administration. The authors would also like to acknowledge the support of the Consortium for Advanced Simulation of LWRs (CASL), also funded by the Department of Energy.

REFERENCES

1. G. YEOH and J. TU, *Computational Techniques for Multiphase Flows -- Basics and Applications*, Butterworth-Heinemann, (2010).
2. M. ISHII and T. HIBIKI, *Thermo-fluid Dynamics of Two-phase Flow*, 2nd ed. Springer, (2011).
3. Y. SATO, M. SADATOMI and K. SEKOGUCHI, "Momentum and heat transfer in two-phase bubble flow-I," *Int. J. Multiphase Flow*, **7**, 167, (1981).
4. A. TROSHKO and Y. HASSAN, "A two-equation turbulence model of turbulent bubbly flows," *Int. J. Multiphase Flow*, **27**, 1965, (2001).
5. M. POLITANO, P. CARRICA and J. CONVERTI, "A model for turbulent polydisperse two-phase flow in vertical channels," *Int. J. Multiphase Flow*, **29**, 1153, (2003).
6. R. RZEHAK and E. KREPPER, "CFD modeling of bubble-induced turbulence," *Int. J. Multiphase Flow*, **55**, 138, (2013).
7. M. COLOMBO, M. FAIRWEATHER, S. LO and A. SPLAWSKI, "Multiphase RANS Simulation of Turbulent Bubbly Flows," *Proc. NURETH-16*, Chicago, IL, USA, (2015).
8. S. WANG, S. LEE, O. JONES and R. LAHEY, "3-D turbulence structure and phase distribution measurements in bubbly two-phase flows," *Int. J. Multiphase Flow*,**13**, 327, (1987).
9. M. SHAWKAT, C. CHING and M. SHOUKRI, "On the liquid turbulence energy spectra in two-phase bubbly flow in a large diameter vertical pipe," *Int. J. Multiphase Flow*, **33**, 300, (2007).
10. A. SERIZAWA and I. KATAOKA, "Turbulence Suppression in Bubbly Two-Phase Flow," *Nuc. Eng. & Des.*, **122**, 1, (1990).
11. T. LIU and S. BANKOFF, "Structure of air-water bubbly flow in a vertical pipe -- I. Liquid mean velocity and turbulence measurements," *Int. J. Heat Mass Transfer*, **36**, 1049, (1993).
12. T. LIU, "Experimental investigation of turbulence structure in two-phase structure in two-phase bubbly flow," Ph.D. Thesis, (1989).
13. M. LANCE and J. BATAILLE, "Turbulence in the liquid phase of a uniform bubbly air-water flow," *J. Fluid Mechanics*, **222**, 95, (1991).
14. J. MERCADO, D. GOMEZ, D. VAN GILS, C. SUN and D. LOHSE, "On bubble clustering and energy spectra in pseudo-turbulence," *J. Fluid Mech.*, **650**, 287, (2010).
15. I. ROGHAIR, J. MERCADO, M. ANNALAND, H. KUIPERS, C. SUN and D. LOHSE, "Energy spectra and bubble velocity distributions in pseudo-turbulence: Numerical simulations vs. experiments," *Int. J. Multiphase Flow*, **37**, 1093, (2011).
16. C. BROWN and I.A. BOLOTNOV, "Spectral analysis of single- and two-phase bubbly DNS in different geometries," *Nuc. Sci. & Eng.*, **184**, (2016).
17. J. LELOUVETEL, T. TANAKA, Y. SATO and Y. HISHIDA, "Transport mechanisms of the turbulent energy cascade in upward/downward bubbly flows," *J. Fluid Mech.*, **741**, 514, (2014).
18. C. SANTARELLI, J. ROUSSEL and J. FROHLICH, "Budget analysis of the turbulent kinetic energy for bubbly flow in a vertical channel," *Chem. Eng. Sci.*, **141**, 46, (2016).
19. A. ESMAEELI and G. TRYGGVASON, "Direct numerical simulations of bubbly flows. Part 2. Moderate Reynolds number arrays," *J. Fluid Mech.*,**385**, 325, (1999).
20. B. BUNNER and G. TRYGGVASON, "Effect of bubble deformation on the stability and properties of bubbly flows," *J. Fluid Mech.*,**495**, 77, (2003).
21. I.A BOLOTNOV, "Influence of bubbles on the turbulence anisotropy," *J. Fluids Eng.*, **135**, (2013).
22. J. LU and G. TRYGGVASON, "Effect of bubble deformability in turbulent bubbly upflow in a vertical channel," *Phys. Fluids*, **20**, (2008).
23. J. LU and G. TRYGGVASON, "Dynamics of nearly spherical bubbles in turbulent channel upflow," *J. Fluid Mech.*, **732**, 166, (2013).
24. J. FANG, M. RASQUIN and I.A. BOLOTNOV, "Interface tracking simulations of bubbly flows in PWR relevant geometries," *Nuc. Eng. & Des.*, (In Press), (2016).
25. M. MING, J. LU and G. TRYGGVASON, "Using statistical learning to close two-fluid multiphase flow equations for bubbly flows in vertical channels," *Int. J. Multiphase Flow*, **85**, 336, (2016).
26. I. KATAOKA and A. SERIZAWA, "Basic equations of turbulence in gas-liquid two-phase flow," *Int. J. Multiphase Flow*, **15**, 843, (1989).
27. I. KATAOKA, K. YOSHIDA, M. NAITOH, H. OKADA, and T. MORII, *Transport of Interfacial Area Concentration in Two-Phase Flow*, In: Mesquita, Amir (Ed.), Nuclear Reactors, InTech, (2012).

28. K. IWAMOTO, Y. SUZUKI, and N. KASAGI, "Reynolds number effect on wall turbulence: toward effective feedback control," *Int. J. Heat and Fluid Flow*, **23**, 678, (2002).